Equation of state of ammonia dihydrate up to 112 GPa by static and dynamic compression experiments in diamond anvil cells

A. Mondal [1], R. J. Husband [2], H.-P. Liermann [2], and C. Sanchez-Valle [1]
[1]*Institut für Mineralogie, Universität Münster, 48149 Münster, Germany*
[2]*Deutsches Elektronen-Synchrotron DESY, Notkestrasse 85, 22607 Hamburg, Germany*

(Received 18 April 2023; revised 7 June 2023; accepted 8 June 2023; published 23 June 2023)

Understanding the high-pressure behavior of ammonia hydrates is relevant for modeling the interior of solar and extrasolar icy bodies. We present here the results of high-pressure x-ray diffraction studies on ammonia-dihydrate (ADH) at room temperature (298 K) up to 112 GPa, employing both static and dynamic compression experiments performed in diamond anvil cells. The derived pressure-volume (*P*-*V*) compression curves are in excellent agreement regardless of the compression technique. In contrast to early theoretical predictions, our results indicate the stability of the disordered molecular alloy (DMA) phase, a body centered cubic (bcc) structure, and the absence of self-ionization in the investigated pressure range. By combining the *P*-*V* data from seven different compression runs, we derive the first equation of state for ADH-DMA based on the third-order Birch-Murnaghan formalism with best-fit parameters: $V_0 = 23.96 \pm 0.03$ (Å^3/molecule), $B_0 = 9.95 \pm 0.14$ GPa, and $B_0' = 6.59 \pm 0.03$. The instantaneous bulk modulus directly derived from the quasicontinuous compression curves displays a smooth increase upon compression that further supports the absence of structural transitions.

DOI: 10.1103/PhysRevB.107.224108

I. INTRODUCTION

Ices of water (H_2O), ammonia (NH_3), and methane (CH_4), and mixtures thereof (hereafter HNCO ices), are thought to be major constituents in planetary bodies from comets to the interiors of the icy moons of the Jovian planets (e.g., Titan and Ganymede) and the solar ice giants (Uranus and Neptune) [1–3]. Most recently, thousands of (exo)planets with sizes between the Earth and Neptune (1–4 R_E, R_E = Earth radius), and whose interiors are likely dominated by HNCO ices (the so-called "mini-Neptunes"), have been identified by space missions like KEPLER, GAIA, and TESSS [4–8]. Knowledge of the structure and physical properties of HNCO ices at relevant high pressure–high temperature conditions (>50 GPa and 1000 K) are thus fundamental to develop accurate models for the internal structure and dynamics of solar and extrasolar icy worlds and to interpret the available geophysical observations [9,10].

The high-pressure behavior of the ammonia (NH_3)–water (H_2O) system is of particular relevance not only to planetary sciences but also as a proxy for systems displaying both homonuclear and heteronuclear hydrogen bonding [11]. Ammonia is readily soluble in water and three stoichiometric ammonia hydrates have been shown to crystallize at low temperatures depending on the initial NH_3:H_2O ratio—ammonia dihydrate (ADH, NH_3:H_2O = 1:2), ammonia monohydrate (AMH, NH_3:H_2O = 1:1), and ammonia hemihydrate (AHH, NH_3:H_2O = 2:1) [12,13]. After the earliest work by Nicol and co-workers [14–16], a number of experimental and theoretical studies have investigated the behavior of NH_3−rich hydrates (>50 wt % NH_3) at high pressure–high temperature conditions. Rich polymorphism [17–20], extensive dehydration reactions [11,17,19], and the formation of partially ionic phases [19–23] at lower pressure conditions than observed for the pure NH_3 [24] have been reported for AMH and AHH to date. Conversely, the experimental data on the H_2O-rich hydrate, ADH, is limited to pressures below 10 GPa [25,26] despite the potential relevance for planetary modeling considering the cosmochemical abundance of ammonia and water, NH_3:H_2O = 1:7 [27].

X-ray diffraction studies on crystalline ADH were performed by Bertie *et al.* [28] who identified the ADH-I phase and determined its crystal structure at 105 K. Further studies employing both x-ray and neutron diffraction techniques revealed a total of five high-pressure polymorphs of ADH below 10 GPa [11,16,25,26,29–31]. The highest pressure polymorph experimentally identified to date, ADH-V, displays a unique body centered cubic (bcc) structure, characterized by a random distribution of NH_3/H_2O molecules and orientational disorder in the protons on all the lattice sites, which is referred to as a disordered molecular alloy (DMA) structure [25,26]. The disordered alloy structure was identified in AMH [32] and later in AHH [17], although most recent studies indicate the partial ionization of the structure [19,20,22,23], thus renaming it a disordered ionicomolecular alloy, DIMA [19,22]. For ADH, first principle molecular dynamic simulations predicted several structural phase transitions upon compression at room temperature, including the transition into a purely ionic tetragonal phase at pressure as low as 12 GPa, and superionicity at temperatures above 1000 K [33–35]. These predictions are yet to be confirmed due to the lack of experimental high pressure–high temperature studies on the ADH-DMA phase beyond 10 GPa.

Here we present the results of room temperature (298 K) x-ray diffraction compression studies on the ADH-DMA phase up to 112 GPa from both static and dynamic

TABLE I. Summary of static (sDAC) and dynamic (dDAC) compression runs performed on the ADH-DMA phase up to 112 GPa at room temperature.

Run	Culet (μm)	Gasket	Sample chamber (μm)	Starting *P* (GPa)	Highest *P* (GPa)	Compression Ttpe
sDAC1	200	Re	100	44	82	static
sDAC2	200	Re	100	26	85	static
sDAC3	200	Re	100	29	78	static
sDAC4	150	Re with amorphous insert	70	52	100	static
dDAC1	150	Re with amorphous insert	70	12	112	dynamic
dDAC2	200	Re with amorphous insert	100	18	55	dynamic
dDAC3	200	Re	100	14	87	dynamic

compression experiments in diamond anvil cells. The dense data coverage of the compression curves obtained here demonstrates the stability of the bcc structure of the ADH-DMA phase lacking evidence for self-ionization up to the highest pressure investigated. Our result provides the first equation of state (EoS) and the pressure dependence of the instantaneous bulk modulus of the ADH-DMA phase at conditions relevant to the midmantle layers of large icy (exo)planets.

II. METHODOLOGY

A. Diamond anvil cell (DAC) techniques

Powder x-ray diffraction measurements were conducted using symmetric piston-cylinder type diamond anvil cells (DACs) equipped with 150–200-μm-diameter culet diamonds (type *Ia*). Rhenium (Re) gaskets preindented to ∼30 μm and drilled with a hole at the center with approximately half of the diamond culet diameter served as sample chambers. In some of the runs, an amorphous metallic glass ($Fe_{0.79}Si_{0.07}B_{0.14}$) insert lining the gasket [36] was employed avoiding parasitic scattering from Re that could overlap with the weak sample reflections.

The ADH-DMA sample investigated here was synthesized using a commercially available NH_3-H_2O solution containing 32 wt% NH_3 (Sigma-Aldrich, product no. 1.05426), which corresponds to the appropriate mixing ratio to stabilize the stoichiometric ADH phase [12]. Because the concentration is close to the room temperature solubility of NH_3 in the system, the solution was refrigerated to ∼278 K to prevent NH_3 evaporation during the loading procedure and the DAC assembly was precooled to ∼292 K before loading. One drop of the solution was placed inside the sample chamber with the help of a medical syringe and the DAC was immediately closed at a pressure below 1 GPa, to avoid sample demixing during crystallization at room temperature [17]. Gold (Au) powder was added to the compression chamber to serve as a pressure marker. Furthermore, the ADH-DMA phase was stabilized at low temperatures following procedures described in earlier studies [25,26,32]. The DAC was placed on a metal stand partially immersed in a liquid N_2 bath to cool down the sample below 160 K. The sample temperature was monitored using an OMEGA thermometer (CL3515R) along with a *K*-type thermocouple attached to the back of one of the diamonds. When the temperature reached ∼150 K, the sample was compressed up to at least 10 GPa to avoid the decomposition of the sample into ice VII and ammonia hemihydrate II (AHH-II) as the cell warms up to room temperature [17]. The initial pressure of the as-synthetized ADH-DMA phase in each run is reported in Table I. X-ray diffraction analysis along with Raman spectroscopic studies prior to the compression experiments confirmed either the formation of the ADH-V or ADH-DMA phase and the absence of other phases such as ice VII or AHH-II in the compression chamber.

A total of seven compression runs were performed up to a maximum pressure of 112 GPa, compressing the sample inside the DAC either statically or dynamically. In the static compression experiments, the sample was pressurized by a gas-driven membrane attached to the upstream side of the DAC. In dynamic compression runs, a symmetric piston-cylinder DAC was inserted in a dDAC assembly containing a high-voltage piezoelectric actuator that expands when voltage is applied resulting in a smooth and continuous pressure increase [37]. The DAC was compressed using a triangular voltage wave form with a rise and fall time of 1200 s each, resulting in an average compression rate of 0.1 GPa/s (e.g., the dDAC1 sample).

B. X-ray diffraction data collection and analysis

Monochromatic synchrotron x-ray beams of either 42.7 (static compression) or 25.6 keV (dynamic compression) with a focal spot size of 2 μm × 2 μm or 3 μm × 8 μm ($H \times V$) full width at half maximum (FWHM), respectively, were employed for powder XRD experiments at the Extreme Condition Beamline P02.2 at PETRA III, DESY, Hamburg [38]. For static compression experiments, data were collected using the flat panel detector XRD1621 from Perkin Elmer equipped with a Ta-doped CsI sensor bonded to an amorphous silicon readout chip. Time-resolved XRD data collection in the dynamic compression experiments was accomplished using 2 × 2.3 MPix GaAs LAMBDA detectors [39,40]. The sample to detector distance, tilt, and rotation of the XRD1621 and LAMBDA detectors were calibrated using CeO_2 and Cr_2O_3 standards (NIST 674b). Typical acquisition times per spectrum were 10 and 2 s for the static and dynamic compression experiments, respectively.

Diffraction images were integrated into one-dimensional (1D) patterns using DIOPTAS software [41] and peak positions of individual reflections were determined based on a fit of a pseudo-Voigt function using a least-squares fitting routine. The lower photon energy and the limited angular coverage by the LAMBDA detector resulted in reduced

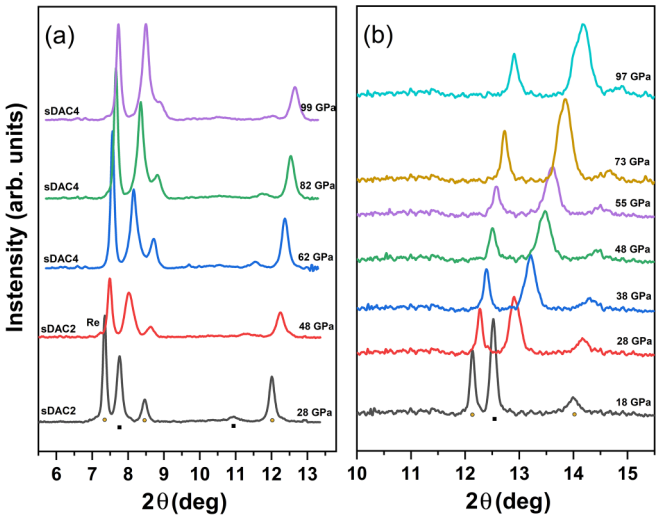

FIG. 1. Selected x-ray diffraction patterns of the ADH-DMA phase recorded upon compression at 298 K in (a) static compression, sDAC2 and sDAC4 samples (incident energy 42.7 keV) and (b) dynamic compression, dDAC1 run (incident energy 25.6 keV). Bragg reflections corresponding to the ADH-DMA phase are marked by black squares. The other major reflections correspond to the gold (Au) pressure marker (yellow circles). Weak Re reflections from the gaskets are also present in some spectra.

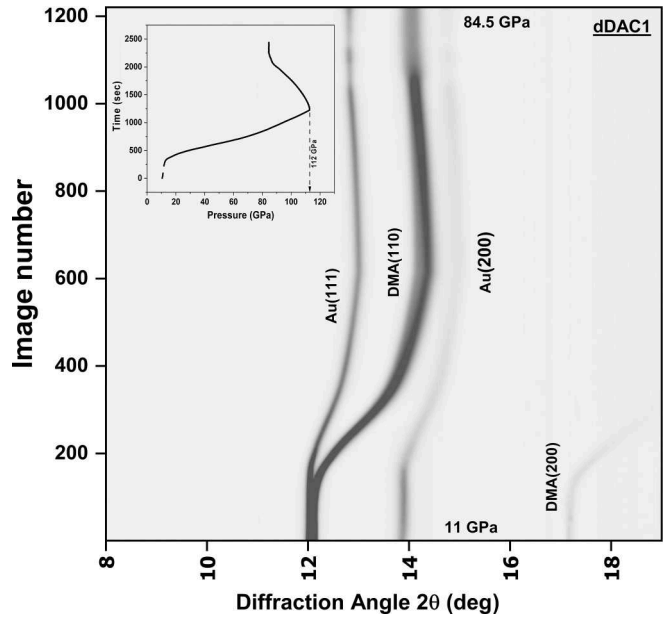

FIG. 2. Intensity plot showing the evolution of diffraction patterns collected for dDAC1 in Image number vs 2θ space. The (110) diffraction line of the ADH-DMA phase is most intense reflection and can be traced over the full compression range. The inset shows the propagation of pressure during the corresponding run. The initial, final, and highest pressure reached during the ramp compression is indicated in the graph.

2θ angle sampling in the dynamic compression experiments compared to the static compression experiments. Therefore, only the (110) reflection of the ADH-DMA bcc structure was observed throughout the entire pressure range (up to 112 GPa) in the dynamic compression experiments, compared to the two to three reflections in the static compression runs (Fig. 1). The reported lattice parameters of the ADH-DMA phase were therefore determined based on the position of the (110) reflection in all runs to allow for a direct comparison between data sets collected using the two different experimental approaches. The validity of this approach was confirmed by the excellent agreement between the lattice parameters and those obtained by Le Bail refinements performed on selected diffraction patterns from the static compression runs. The uncertainty in the ADH-DMA volume was estimated based on the standard deviation in the volumes determined from the (110) and (200) reflections in the static compression experiments and assumed to be similar for the dynamic compression data as this approach cannot be applied. The pressure was estimated based on the peak position of the Au (111) reflection, which was previously shown to be least affected by the presence of nonhydrostatic uniaxial stress [42]. The bulk modulus from the pressure-volume data was obtained by fitting the dataset to a third order Birch-Murnaghan equation of state (BM EoS) and by numerical differentiation of the pressure-volume (P-V) compression curve on account of the data coverage achieved here.

III. RESULTS AND DISCUSSION

A. Pressure evolution of ADH-DMA phase to Mbar pressures

Figure 1 shows selected diffractograms collected during static (sDAC2 and sDAC4, Table I) and dynamic (dDAC1, Table I) compression experiments, whereas the time evolution of the diffractograms during the entire compression cycle in a dynamic compression experiment (dDAC1, Table I) is shown in Fig. 2. Additional data from the static and dynamic compression experiments are reported in Figs. S1 and S2, respectively, of the Supplemental Material [43]. The characteristic (110) reflection of the bcc ADH-DMA phase was generally the most intense diffraction line observed up to the highest pressure and could be resolved without overlap with the gasket signal because of the use of metallic glass inserts [36]. Weak signals arising from the Re gasket are however observed in the diffraction patterns from samples that were not prepared with metallic glass inserts (Fig. 1 and Fig. S1 of the Supplemental Material [43]). Whenever there was a large overlap between the sample signal and diffraction from the Re gasket or the Au pressure marker, the diffractograms were rejected from further analysis. Le Bail refinements performed on selected patterns from static compression run sDAC2 (Fig. 3) confirm that all diffraction lines which are not from the Au pressure marker or the Re gasket can be indexed based on the bcc structure (space group $Im{-}3m$) proposed by earlier lower-pressure studies [25,26]. These observations confirm the lack of structural transitions in the ADH-DMA phase up to the highest pressure investigated here.

The stability of bcc ADH-DMA phase in the investigated pressure range is in contrast with the results from previous theoretical studies on ADH and the behavior reported for other ammonia hydrate phases [19,20,22,23]. First principle molecular dynamic simulations predicted the transition of molecular ADH-DMA into an ionic phase with a tetragonal structure

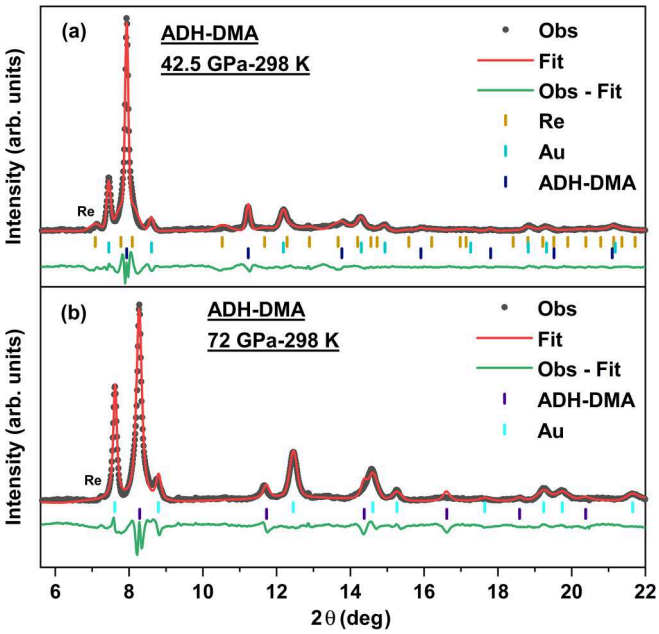

FIG. 3. X-ray diffraction pattern of ADH-DMA phase at (a) 42.5 GPa and (b) 72 GPa at room temperature (run sDAC1). The black circles are experimental data and the red line is the Le Bail refinement fit. Colored sticks show the position of the Bragg reflections for the sample, the Re gasket, and the Au pressure calibrant correspondingly. The green line represents the difference between observed and calculated profile patterns. The goodness of fit parameters are as follows: (a) $R_{wp} = 0.3321$, $R_p = 0.1825$, $\chi^2 = 1.014$, and (b) $R_{wp} = 0.4735$, $R_p = 0.2146$, $\chi^2 = 2$.

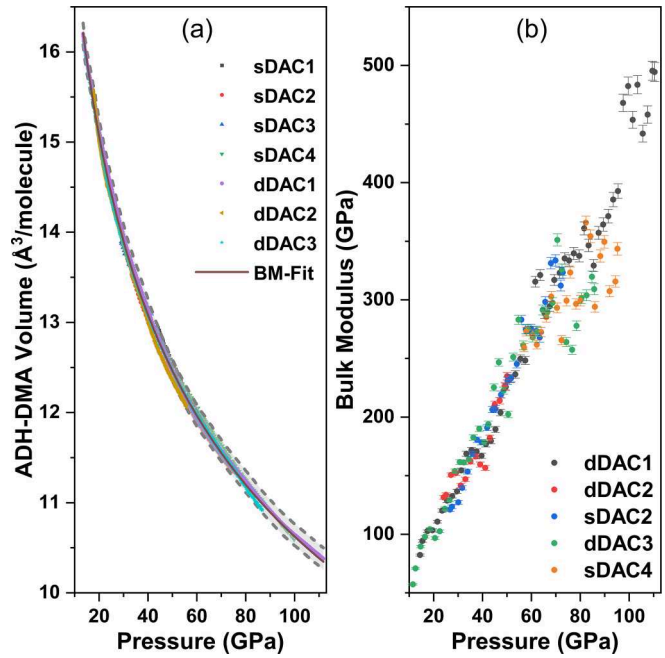

FIG. 4. (a) Pressure-volume data for the ADH-DMA phase obtained in all static (four runs) and dynamic (three runs) compression experiments. Data from all runs are in excellent agreement and fall within the error envelop (grey shadowed area) outlined by the grey dashed line. The solid line represents a joint fit to all datasets by a third order Birch-Murnaghan EoS. (b) Pressure evolution of the instantaneous bulk modulus of the ADH-DMA phase calculated directly by numerical differentiation of the *P-V* curve, $B = -V\,\frac{dP}{dV}$, for selected static and dynamic compression runs. The smaller volume changes (dV) as the material densifies result in higher fluctuations in the instantaneous bulk modulus in the high-pressure range.

($I4_1cd$) at 12 GPa [33], while orthorhombic ($Ama2$) and monoclinic ($P2_1/m$) structures are subsequently stabilized upon further compression [34,35]. Similarly, recent x-ray diffraction and Raman spectroscopy studies on AMH have also shown the coexistence of the bcc DIMA phase with a purely ionic ordered tetragonal ($P4/mnn$) structure solely composed of NH_4^+ and OH^- above 8 GPa [19,22], in agreement with early theoretical predictions [21]. Moreover, the spontaneous ionization of the ammonia hemihydrate DMA phase above 26 GPa has been observed by both Raman spectroscopy and first principle calculations [23]. To further confirm the absence of transition towards ionic structures in ADH, we have simulated the XRD patterns of the predicted ionic high-pressure phases ($I4_1cd$, $Ama2$ and $P2_1/m$) [33,34] and compared them to the spectra recorded at similar pressure conditions (Figs. S3–S5) [43]. We note the absence of the characteristic reflections of the ionic phases in our XRD data and emphasize that, if present, they could be resolved from those of ADH-DMA and the Au standard. Moreover, we systematically recorded x-ray diffraction maps across the sample chamber before and after the static compression runs as the ionic phases may not be uniformly distributed in the sample [22]. The maps rule out the presence of ammonia-bearing phases other than ADH-DMA in the sample chamber and thus confirm the lack of transition toward ionic structures in ADH-DMA in the present study. The persistence of the molecular phase of ADH upon compression points to distinct compressional behavior of the ADH-DMA phase compared to other ammonia hydrates. Nevertheless, additional Raman spectroscopy analysis, which is more sensitive to the presence of ionic species than x-ray diffraction [19], will be required to confirm the observations.

B. $P - V$ compression curve of ADH-DMA

The pressure evolution of the ADH-DMA volume (per molecule) derived from data collected in all static and dynamic compression runs is shown in Fig. 4(a). Overall, the volume measured in static and dynamic compression runs agrees well within its uncertainties. The *P-V* data from all the runs along with their error was fit to a third order Birch-Murnaghan equation of state (BM EoS) using EOSFIT7C program [44] to derive the volume (per molecule) V_0, the bulk modulus B_0, and its pressure derivative B_0' at ambient conditions. Initially, the ambient volume V_0 of the ADH phase was estimated considering an ideal mixture of NH_3 and H_2O with a 1:2 molar ratio which was then refined during the fitting procedure. The best-fit EoS parameters for ADH-DMA are $V_0 = 23.96 \pm 0.03$ (Å^3/molecule), $B_0 = 9.95 \pm 0.14$ GPa, and $B_0' = 6.59 \pm 0.03$ (Table II). The entire *P-V* data set is well described by a single equation of state [Fig. 4(a)], whose extrapolation to low pressure is in excellent agreement with earlier data [25,26] (Fig. 5). To validate the choice of the EoS fit model, we computed the Eulerian strain (f_E) and normalized stress (F_E) for the dDAC1 data and plotted them in

TABLE II. Equation of state parameters for ice phases in the NH_3-H_2O system.

Compound	ADH-DMA (BM EoS, this work)	AMH-DIMA (BM EoS) [48]	H_2O (BM EoS) [50]	NH_3 (Vinet EoS) [51]
V_0 (Å^3/molecule)	23.96 ± 0.03	25.933 ± 0.027	21.12 ± 0.15	33.0 ± 0.8
B_0 (GPa)	9.95 ± 0.14	12.166 ± 0.051	13.8 ± 0.2	7.10 ± 0.11
B_0'	6.59 ± 0.03	5.3 ± 0 (fixed)	5.9 ± 0.1	5.97 ± 0.20
χ^2	0.23[a]			3.98

[a]The goodness of the fit is represented by the weighted χ^2 parameter.

a *f-F* plot [45,46]. A linear fit over the entire data set confirms the refined B_0 value and its large pressure derivative, $B_0' > 4$ (Fig. S6) [43].

The dense x-ray diffraction data coverage in both static and dynamic compression experiments performed here also permit the derivation of the instantaneous bulk modulus by numerical differentiation of the $P-V$ compression curve, $B = -V\frac{dP}{dV}$, without resorting to an EoS. This parameter is a very sensitive proxy for structural transitions as shown in a recent dynamic compression study of pure H_2O where the ice VII, ice VII′, and ice X′ structural transitions could be identified by softening in the bulk modulus between 35 and 65 GPa [47]. We thus adopted the method described by Méndez *et al.* [47] and reduced our dense data set by considering data points with ∼2 GPa pressure intervals while preserving the main features of the dataset (Fig. S7 [43]). The pressure dependence of the instantaneous bulk modulus calculated from five different data sets is shown in Fig. 4(b). All data sets are in good agreement with each other, further supporting the idea that the pressure-dependent compressibility is independent of the compression rate. Moreover, the instantaneous bulk modulus shows an almost linear increase within the investigated pressure range. The absence of softening and the smooth increase on the pressure-dependent instantaneous bulk modulus thus provide further support for the stability of the bcc structured ADH-DMA phase up to 112 GPa, in contrast to the theoretical predictions [33–35].

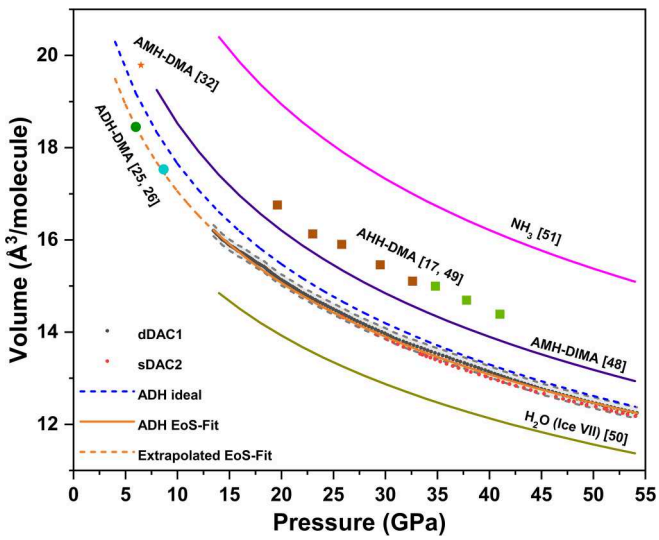

FIG. 5. Comparison of the compression curves of DMA/DIMA phases in the NH_3-H_2O system. Grey shadowed area outlined by the grey dashed line indicates the error envelope in our ADH-DMA experimental data. Experimentally obtained ADH-DMA phase volumes do not match the calculated ADH-DMA volume assuming ideal mixing between NH_3 and H_2O with 1:2 mixing ratio (ADH ideal).

C. Comparison with other ice phases in the NH_3-H_2O system

Figure 5 compares the *P-V* data for ADH-DMA to the available data of the DIMA phases formed in other ammonia hydrates, AMH [32,48] and AHH [17,49], and the end members H_2O (ice VII) [50] and NH_3 [51]. The volume (per molecule) for DMA/DIMA phases with different stoichiometric ratios of NH_3 and H_2O lie in between the two end members, H_2O and NH_3, and gradually *increases* with the NH_3 content at constant pressure. However, we note that the *P-V* curve calculated for an $NH_3 : 2H_2O$ hydrate assuming linear mixing in volume (ADH ideal) slightly deviates from the experimental data for ADH-DMA. We ascribe the departure from the ideal volume to the complexity of the H-bonding network which prevents the arrangement of all O(N)-H bonds along the same lattice plane [32]. Differences between the experimental and calculated volumes decrease as pressure increases, suggesting that ideal behavior may be approached at high pressure. The bulk modulus B_0 and its pressure derivative B_0' determined for ADH-DMA compare well with those previously reported for other ice phases in the NH_3-H_2O system (Table II), including AMH-DIMA [48] and the end members H_2O (ice VII) [50] and NH_3 [51]. All phases display B_0' values greater than 4, indicating rapid densification of the material upon compression. The bulk modulus B_0 of ADH-DMA is closer to that of H_2O ice VII than NH_3, consistent with its higher H_2O content.

IV. CONCLUSION

We have investigated the compressional behavior of the ADH-DMA phase up to 112 GPa by means of powder x-ray diffraction coupled with static and dynamically compressed diamond anvil cells. Le Bail refinements confirm that all ADH reflections can be indexed based on the bcc structure as proposed by previous low-pressure studies (<10 GPa). Our detailed investigation thus confirms the stability of the bcc ADH-DMA phase up to 112 GPa and rules out the occurrence of structural transitions, including towards ionic structures, predicted by theory. The *P-V* compression curves derived from static and dynamic compression experiments are in excellent agreement within uncertainties. A

joint fit to all *P-V* data sets by a third order BM EoS yields the best-fit parameters: $V_0 = 23.96 \pm 0.03$ (Å^3/molecule), $B_0 = 9.95 \pm 0.14$ GPa, and $B_0' = 6.59 \pm 0.03$. The volume (per molecule) of ADH-DMA is closer to that of H_2O (ice VII) than to NH_3 over the entire compression range, consistent with the higher H_2O content of the hydrate, while the B_0 and B_0' values compare well with those reported for other hydrogen-bonded phases. The instantaneous bulk modulus derived for both static and dynamic compression runs are in good agreement and display a smooth increase with pressure which further supports the absence of structural transitions. The lack of self-ionization upon compression in ADH-DMA is in contrast with the behavior of other ammonia hydrates, i.e., AMH and AHH, suggesting differences in the pressure response of the hydrogen bonding network in low-ammonia content hydrates.

ACKNOWLEDGMENTS

This research was supported by the German Science Foundation (Deutsche Forschungsgemeinschaft, DFG) through Research Unit FOR 2440/2 (Grant No. SA2585/5-1). We acknowledge DESY (Hamburg, Germany), a member of the Helmholtz Association, for providing access to the experimental facility PETRA III and beamline P02.2. We also want to thank K. Glazyrin and M. French for helpful discussions and P02.2 beamline engineers M. Wendt and S. Wenz for their useful support.

[1] W. B. Hubbard, Interiors of the giant planets, Science **214**, 145 (1981).
[2] T. Guillot, Condensation of methane, ammonia, and water and the inhibition of convection in giant planets, Science **269**, 1697 (1995).
[3] H. Hussmann, C. Sotin, and J. I. Lunine, Interiors and evolution of icy satellites, in *Treatise on Geophysics*, 2nd ed., edited by G. Schubert (Elsevier, New York, 2015), Vol. 10, pp. 605–635.
[4] W. J. Borucki, D. Koch, G. Basri, N. Batalha, T. Brown, D. Caldwell, J. Caldwell, J. Christensen-Dalsgaard, W. D. Cochran, E. Devore, E. W. Dunham *et al.*, Kepler planet-detection mission: Introduction and first results, Science **327**, 977 (2010).
[5] W. J. Borucki, E. Agol, F. Fressin, L. Kaltenegger, J. Rowe, H. Isaacson, D. Fischer, N. Batalha, J. J. Lissauer, G. W. Marcy, D. Fabrycky *et al.*, Kepler-62: A five-planet system with planets of 1.4 and 1.6 earth radii in the habitable zone, Science **340**, 587 (2013).
[6] J. J. Lissauer, D. C. Fabrycky, E. B. Ford, W. J. Borucki, F. Fressin, G. W. Marcy, J. A. Orosz, J. F. Rowe, G. Torres, W. F. Welsh, N. M. Batalha *et al.*, A closely packed system of low-mass, low-density planets transiting Kepler-11, Nature (London) **470**, 53 (2011).
[7] E. J. Rivera, J. J. Lissauer, R. P. Butler, G. W. Marcy, S. S. Vogt, D. A. Fischer, T. M. Brown, G. Laughlin, and G. W. Henry, A $\sim$7.5M$_\oplus$ planet orbiting the nearby star, GJ 876, Astrophys. J. **634**, 625 (2005).
[8] N. M. Batalha, J. F. Rowe, S. T. Bryson, T. Barclay, C. J. Burke, D. A. Caldwell, J. L. Christiansen, F. Mullally, S. E. Thompson, T. M. Brown, A. K. Dupree *et al.*, Planetary candidates observed by kepler. III. analysis of the first 16 months of data, Astrophys. J., Suppl. Ser. **204**, 24 (2013).
[9] J. J. Fortney and N. Nettelmann, The interior structure, composition, and evolution of giant planets, Space Sci. Rev. **152**, 423 (2010).
[10] R. Helled, J. D. Anderson, M. Podolak, and G. Schubert, Interior models of uranus and neptune, Astrophys. J. **726**, 15 (2010).
[11] J. S. Loveday and R. J. Nelmes, The ammonia hydrates—model mixed-hydrogen-bonded systems, High Press. Res. **24**, 45 (2004).
[12] J. S. Kargel, Ammonia-water volcanism on icy satellites: Phase relations at 1 atmosphere, Icarus **100**, 556 (1992).
[13] A. D. Fortes and M. Choukroun, Phase behaviour of ices and hydrates, Space Sci. Rev. **153**, 185 (2010).
[14] M. L. Johnson and M. Nicol, The ammonia-water phase diagram and its implications for icy satellites, J. Geophys. Res. Solid Earth **92**, 6339 (1987).
[15] H. C. Cynn, S. Boone, A. Koumvakalis, M. Nicol, and D. J. Stevenson, Phase diagram for ammonia-water mixtures at high pressures: Implications for icy satellites, in *Proceedings of 19th Lunar and Planetary Science Conference* (Lunar and Planetary Institute, Houston, TX, 1989), pp. 433–441.
[16] S. Boone and M. F. Nicol, Ammonia-water mixtures at high pressures - Melting curves of ammonia dihydrate and ammonia monohydrate and a revised high-pressure phase diagram for the water-rich region, Lunar. Planet. Sci. Conf. **21**, 603 (1991).
[17] C. W. Wilson, C. L. Bull, G. W. Stinton, D. M. Amos, M. E. Donnelly, and J. S. Loveday, On the stability of the disordered molecular alloy phase of ammonia hemihydrate, J. Chem. Phys. **142**, 094707 (2015).
[18] V. N. Robinson, Y. Wang, Y. Ma, and A. Hermann, Stabilization of ammonia-rich hydrate inside icy planets, Proc. Natl Acad. Sci. **114**, 9003 (2017).
[19] H. Zhang, F. Datchi, L. M. Andriambariarijaona, G. Zhang, J. A. Queyroux, K. Béneut, M. Mezouar, and S. Ninet, Melting curve and phase diagram of ammonia monohydrate at high pressure and temperature, J. Chem. Phys. **153**, 154503 (2020).
[20] H. Zhang, F. Datchi, L. Andriambariarijaona, M. Rescigno, L. E. Bove, S. Klotz, and S. Ninet, Observation of a plastic crystal in water–ammonia mixtures under high pressure and temperature, J. Phys. Chem. Lett. **14**, 2301 (2023).
[21] G. I. Griffiths, A. D. Fortes, C. J. Pickard, and R. J. Needs, Crystal structure of ammonia dihydrate II, J. Chem. Phys. **136**, 174512 (2012).
[22] C. Liu, A. Mafety, J. A. Queyroux, C. W. Wilson, H. Zhang, K. Béneut, G. Le Marchand, B. Baptiste, P. Dumas, G. Garbarino, F. Finocchi, J. S. Loveday, F. Pietrucci, A. M. Saitta, F. Datchi, and S. Ninet, Topologically frustrated ionisation in a water-ammonia ice mixture, Nat. Commun. **8**, 1065 (2017).
[23] W. Xu, V. N. Robinson, X. Zhang, H.-C. Zhang, M.-E. Donnelly, P. Dalladay-Simpson, A. Hermann, X.-D. Liu, and E. Gregoryanz, Ionic Phases of Ammonia-Rich Hydrate at High Densities, Phys. Rev. Lett. **126**, 015702 (2021).

[24] S. Ninet, F. Datchi, P. Dumas, M. Mezouar, G. Garbarino, A. Mafety, C. J. Pickard, R. J. Needs, and A. M. Saitta, Experimental and theoretical evidence for an ionic crystal of ammonia at high pressure, Phys. Rev. B **89**, 174103 (2014).

[25] A. D. Fortes, I. G. Wood, M. Alfredsson, L. Vočadlo, K. S. Knight, W. G. Marshall, M. G. Tucker, and F. Fernandez-Alonso, The high-pressure phase diagram of ammonia dihydrate, High Press. Res. **27**, 201 (2007).

[26] J. S. Loveday, R. J. Nelmes, C. L. Bull, H. E. Maynard-Casely, and M. Guthrie, Observation of ammonia dihydrate in the AMH-VI structure at room temperature – possible implications for the outer solar system, High Press. Res. **29**, 396 (2009).

[27] M. Asplund, N. Grevesse, A. J. Sauval, and P. Scott, The chemical composition of the Sun, Annu. Rev. Astron. Astrophys. **47**, 481 (2009).

[28] J. E. Bertie and M. R. Shehata, Ammonia dihydrate: Preparation, x-ray powder diffraction pattern and infrared spectrum of $NH_3 \cdot 2H_2O$ at 100 K, J. Chem. Phys. **81**, 27 (1984).

[29] D. L. Hogenboom, J. S. Kargel, G. J. Consolmagno, T. C. Holden, L. Lee, and M. Buyyounouski, The ammonia–water system and the chemical differentiation of icy satellites, Icarus **128**, 171 (1997).

[30] A. D. Fortes, I. G. Wood, J. P. Brodholt, M. Alfredsson, L. Vočadlo, G. S. Mcgrady, and K. S. Knight, A high-resolution neutron powder diffraction study of ammonia dihydrate ($ND_3 \cdot 2D_2O$) phase I, J. Chem. Phys. **119**, 10806 (2003).

[31] A. D. Fortes, I. G. Wood, J. P. Brodholt, and L. Vočadlo, The structure, ordering and equation of state of ammonia dihydrate ($NH_3 \cdot 2H_2O$), Icarus **162**, 59 (2003).

[32] J. S. Loveday and R. J. Nelmes, Ammonia Monohydrate VI: A Hydrogen-Bonded Molecular Alloy, Phys. Rev. Lett. **83**, 4329 (1999).

[33] X. Jiang, X. Wu, Z. Zheng, Y. Huang, and J. Zhao, Ionic and superionic phases in ammonia dihydrate $NH_3 \cdot 2H_2O$ under high pressure, Phys. Rev. B **95**, 144104 (2017).

[34] V. N. Robinson, M. Marques, Y. Wang, Y. Ma, and A. Hermann, Novel phases in ammonia-water mixtures under pressure, J. Chem. Phys. **149**, 234501 (2018).

[35] V. N. Robinson and A. Hermann, Plastic and superionic phases in ammonia–water mixtures at high pressures and temperatures, J. Phys.: Condens. Matter **32**, 184004 (2020).

[36] W. Dong, K. Glazyrin, S. Khandarkhaeva, T. Fedotenko, J. Bednarčík, E. Greenberg, L. Dubrovinsky, N. Dubrovinskaia, and H. P. Liermann, $Fe_{0.79}Si_{0.07}B_{0.14}$ metallic glass gaskets for high-pressure research beyond 1 Mbar, J. Synchrotron Radiat. **29**, 1167 (2022).

[37] Z. Jenei, H. P. Liermann, R. Husband, A. S. Méndez, D. Pennicard, H. Marquardt, E. F. O. Bannon, A. Pakhomova, Z. Konopkova, K. Glazyrin, M. Wendt *et al.*, New dynamic diamond anvil cells for tera-pascal per second fast compression x-ray diffraction experiments, Rev. Sci. Instrum. **90**, 065114 (2019).

[38] H. P. Liermann, Z. Konôpková, W. Morgenroth, K. Glazyrin, J. Bednarčik, E. E. Mcbride, S. Petitgirard, J. T. Delitz, M. Wendt, Y. Bican, and A. Ehnes, The extreme conditions beamline P02.2 and the extreme conditions science infrastructure at PETRA III, J. Synchrotron Radiat. **22**, 908 (2015).

[39] D. Pennicard, S. Lange, S. Smoljanin, H. Hirsemann, H. Graafsma, M. Epple, M. Zuvic, M. O. Lampert, T. Fritzsch, and M. Rothermund, The LAMBDA photon-counting pixel detector, J. Phys.: Conf. Ser. **425**, 062010 (2013).

[40] D. Pennicard, S. Smoljanin, F. Pithan, M. Sarajlic, A. Rothkirch, Y. Yu, H. P. Liermann, W. Morgenroth, B. Winkler, Z. Jenei, H. Stawitz, J. Becker, and H. Graafsma, LAMBDA 2M GaAs—A multi-megapixel hard X-ray detector for synchrotrons, J. Instrum. **13**, C01026 (2018).

[41] C. Prescher and V. B. Prakapenka, DIOPTAS: A program for reduction of two dimensional X-ray diffraction data and data exploration, High Press. Res. **35**, 223 (2015).

[42] K. Takemura and A. Dewaele, Isothermal equation of state for gold with a He-pressure medium, Phys. Rev. B **78**, 104119 (2008).

[43] See Supplemental Material at http://link.aps.org/supplemental/10.1103/PhysRevB.107.224108 for diffraction patterns from additional static and dynamic compression experiments, comparison with theoretically predicted structures, f-F plot, and details of data treatment.

[44] J. Gonzalez-Platas, M. Alvaro, F. Nestola, and R. Angel, EosFit7-GUI: A new graphical user interface for equation of state calculations, analyses and teaching, J. Appl. Crystallogr. **49**, 1377 (2016).

[45] R. J. Angel, Equations of state, Rev. Mineral. Geochem. **41**, 35 (2000).

[46] D. L. Heinz and R. Jeanloz, The equation of state of the gold calibration standard, J. Appl. Phys. **55**, 885 (1984).

[47] A. S. Méndez, F. Trybel, R. J. Husband, G. Steinle-Neumann, H. P. Liermann, and H. Marquardt, Bulk modulus of H_2O across the ice VII–ice X transition measured by time-resolved x-ray diffraction in dynamic diamond anvil cell experiments, Phys. Rev. B **103**, 064104 (2021).

[48] H. Zhang, Experimental investigation of the phase diagram of ammonia monohydrate at high pressure and temperature, Ph.D. thesis, HAL Sorbonne Université, 2019, https://theses.hal.science/tel-03459424.

[49] C. Ma, F. Li, Q. Zhou, F. Huang, J. Wang, M. Zhang, Z. Wang, and Q. Cui, Ammonia molecule rotation of pressure-induced phase transition in ammonia hemihydrates $2NH_3.H_2O$, RSC Adv. **2**, 4920 (2012).

[50] S. Klotz, K. Komatsu, H. Kagi, K. Kunc, A. Sano-Furukawa, S. Machida, and T. Hattori, Bulk moduli and equations of state of ice VII and ice VIII, Phys. Rev. B **95**, 174111 (2017).

[51] F. Datchi, S. Ninet, M. Gauthier, A. M. Saitta, B. Canny, and F. Decremps, Solid ammonia at high pressure: A single-crystal x-ray diffraction study to 123 GPa, Phys. Rev. B **73**, 174111 (2006).